



# Competitive Registration Fields for The Development of Complex Block Copolymer Structures by A Layer-by-Layer Approach

Nils Demazy, Pablo G Argudo, Guillaume Fleury

## ► To cite this version:

Nils Demazy, Pablo G Argudo, Guillaume Fleury. Competitive Registration Fields for The Development of Complex Block Copolymer Structures by A Layer-by-Layer Approach. *Small*, In press, 10.1002/smll.202205254 . hal-03981255

HAL Id: hal-03981255

<https://hal.science/hal-03981255>

Submitted on 9 Feb 2023

**HAL** is a multi-disciplinary open access archive for the deposit and dissemination of scientific research documents, whether they are published or not. The documents may come from teaching and research institutions in France or abroad, or from public or private research centers.

L'archive ouverte pluridisciplinaire **HAL**, est destinée au dépôt et à la diffusion de documents scientifiques de niveau recherche, publiés ou non, émanant des établissements d'enseignement et de recherche français ou étrangers, des laboratoires publics ou privés.

# **Competitive registration fields for the development of complex block copolymer structures by a layer-by-layer approach**

Nils Demazy,<sup>1</sup> Pablo G. Argudo,<sup>1</sup> Guillaume Fleury<sup>1,\*</sup>

<sup>1</sup>Univ. Bordeaux, CNRS, Bordeaux INP, LCPO, UMR 5629, F-33600, Pessac, France.

E-mail: [gfleury@enscbp.fr](mailto:gfleury@enscbp.fr)

**Keywords:** block copolymer, thin film self-assembly, multilayered structures

**Abstract.** Block copolymer (BCP) self-assembly in thin film is an elegant method to generate nanometric features with tunable geometrical configurations. By combining directed assembly and hybridization methods, advances in nano-manufacturing have been attested over the past decades with flagship applications in lithography and optics. Nevertheless, the range of geometrical configurations is limited by the accessible morphologies inherent to the energy minimization process involved in BCP self-assembly. Layering of nanostructured BCP thin films has been recently proposed in order to enrich the span of nanostructures derived from BCP self-assembly with the formation of non-native heterostructures such as double-layered arrays of nanowires or dots-on-line and dots-in-hole hierarchical structures. In this work, we further exploited the layer-by-layer method for the generation of nano-mesh arrays using nanostructured BCP thin films. In particular, we leveraged a subtle combination of chemical and topographical fields in order to demonstrate design rules for the controlled registration of a BCP layer on top of an underneath immobilized one by the precise tuning of the interfacial chemical field between the two BCP layers.

## 1 Introduction

Block copolymer (BCP) self-assembly in thin films is a powerful method to pattern surfaces at the nanometer scale with applications in optics, lithography and advanced nano-manufacturing.<sup>[1–4]</sup> Indeed, the thermodynamic incompatibility between the different chemical sequences in a BCP architecture leads to a phase separation that results in the formation of ordered nanostructures.<sup>[5]</sup> For the most common diblock architecture, the variation of the volume fraction of the blocks leverages the formation of spherical, cylindrical, gyroid and lamellar structures for which the domain spacing is primarily controlled by the degree of polymerization of the BCP chain. Application of block copolymer self-assembly in a thin film configuration further enabled surface texturation<sup>[6,7]</sup> which can be combined by hybridization methods generating hybrid patterns with exquisite symmetries.<sup>[8]</sup> Nevertheless, the geometric features inherent to BCP self-assembly are limited and methods to enrich the breadth of features achievable by BCP self-assembly in thin film are of tremendous interest. A promising method is based on the stacking of BCP layers for which an interplay between the stacked BCP layers based on chemical or topographical constraints is expected to enable a fine control the resulting patterns.<sup>[9–12]</sup> Several methodologies; i.e. use of a protective layer between the stacked nanostructured BCP films,<sup>[13,14]</sup> direct stacking of BCP structures leveraged by immobilization methods,<sup>[15–21]</sup> use of cross-linkable BCP materials,<sup>[22,23]</sup> and transfer printing of BCP films,<sup>[24,25]</sup> have been employed for the formation of customized 3D layered BCP structures. Among these methods, some capitalize on the topographical or chemical fields induced by an underlying (immobilized) BCP film in order to direct the self-assembly of a subsequent BCP layer. This so-called “responsive-layering” approach<sup>[17]</sup> further benefit from the “soft condensed matter” characteristics of BCP self-assembly which affords the formation of complex three-dimensional structures due to spatial confinement or interfacial effects.<sup>[1,26,27]</sup> In

particular, Rahman *et al.*<sup>[17]</sup> reported a large range of non-native BCP nanostructures derived from common diblock morphologies using a responsive layering approach based on topographical fields. Another demonstration of “responsive layering” by Jin *et al.*<sup>[18,28]</sup> leveraged the epitaxial registration of sphere-forming PS-*b*-PDMS monolayers for the formation of Moiré superstructures.

Herein, we further developed the use of the layer-by-layer method for the generation of nano-mesh arrays using nanostructured polystyrene-*b*-poly(methyl methacrylate) (PS-*b*-PMMA) thin films. In particular, we leveraged a subtle combination of chemical and topographical fields in order to demonstrate design rules for the controlled registration of a BCP layer on top of an underneath immobilized one by the precise tuning of the interfacial chemical field between the two BCP layers. This study expands the breadth of control for the registration of stacked BCP layers by interplaying chemo-epitaxy and grapho-epitaxy approaches.

## 2 Results and discussion

In this section, we first discuss the phase behavior of nearly symmetric PS-*b*-PMMA in a thin film configuration in order to define the range of compositions of styrene and methyl methacrylate statistical copolymers, denoted PS-*stat*-PMMA, leading to an out-of-plane orientation of PS-*b*-PMMA lamellae. Indeed, substrates modified by grafted PS-*stat*-PMMA chains enable the modification of the wetting properties of nanostructured PS-*b*-PMMA films by adjusting the interfacial energy of the substrate with respect to the BCP domains.<sup>[29]</sup> This, in turn, allows controlling the orientation of the BCP structure with respect to the substrate plane.<sup>[30,31]</sup> This systematic study is central for further iterative self-assembly as it allows the definition of “slightly” PMMA- or PS- affine and “fully” neutral interfacial layers while preserving the out-of-plane

orientation of the lamellar BCP features. A PS-*b*-PMMA BCP ( $M_n^{\text{PS}} = 27 \text{ kg.mol}^{-1}$ ,  $M_n^{\text{PMMA}} = 22 \text{ kg.mol}^{-1}$ ,  $f_{\text{PS}} = 0.55$ ,  $D = 1.07$ , hereafter named L28) with a domain spacing,  $L_0 = 28 \text{ nm}$ , was self-assembled on Si substrates modified by grafted PS-*stat*-PMMA chains with compositions,  $f_{\text{PS}}$ , ranging from 0.47 to 0.86. After spin-coating, a thermal annealing treatment at 250 °C during 10 min was performed using a rapid thermal annealing (RTA) process. The BCP film thickness evaluated after the spin-coating step,  $t$ , was varied between  $0.5L_0 \approx 15 \text{ nm}$  and  $3L_0 \approx 82 \text{ nm}$ , and representative AFM images are presented in **Figure 1** for  $t/L_0 \approx 1.25$  and various  $f_{\text{PS}}$  (larger AFM phase images are provided in **Figure S1**).

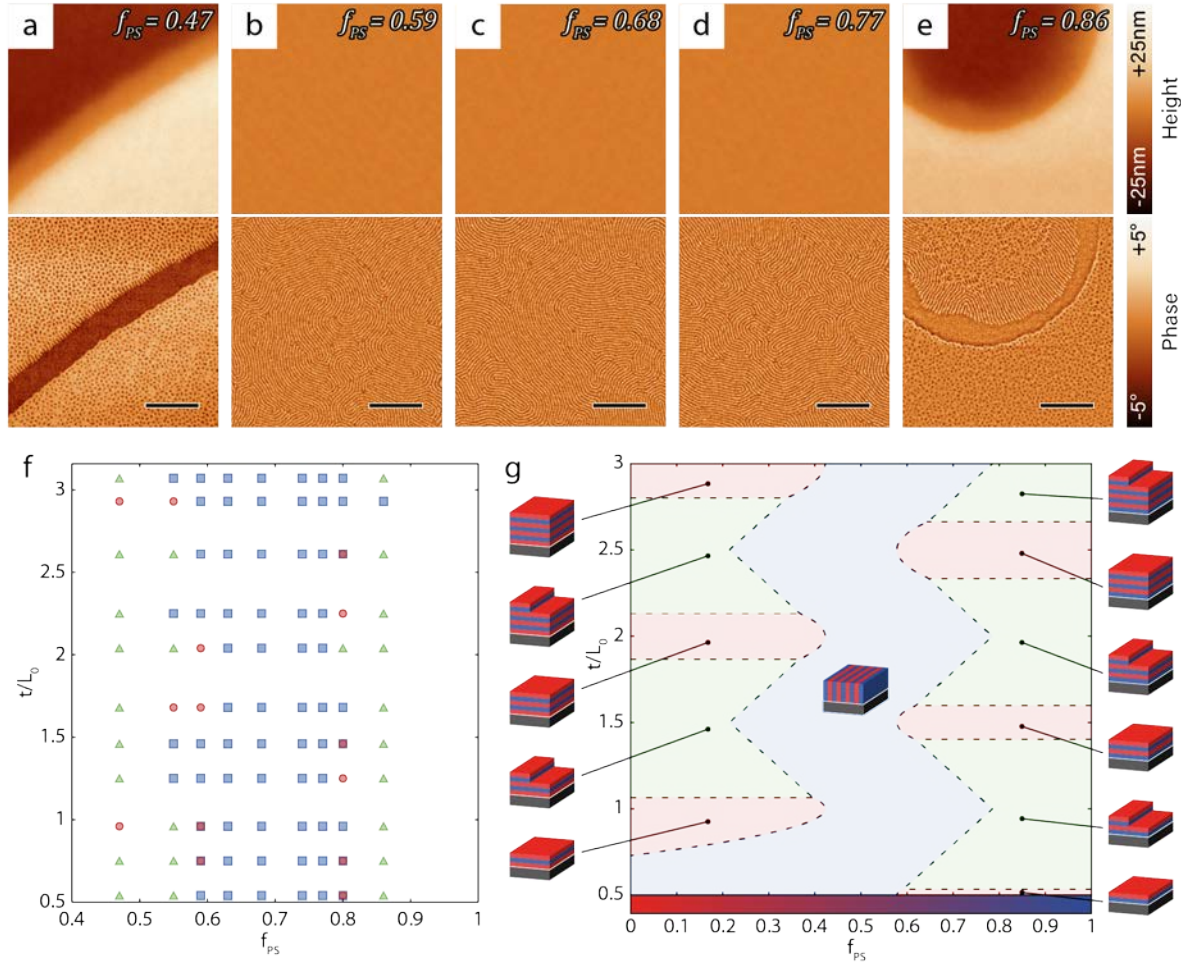


**Figure 1.** (a-e) AFM images (top panel: height images, bottom panel: phase images) of nanostructured *L*28 thin films on Si substrates modified by grafted PS-*stat*-PMMA chains for  $t/L_0 \approx 1.25$ . Scale bars: 500 nm. (a, e) island/hole structures ( $f_{\text{PS}} = 0.47$  and 0.86), (b, c, d) out-of-plane lamellae ( $f_{\text{PS}} = 0.59$ , 0.68 and 0.77). (f) Experimental phase diagram and (g) mapping of the different lamellar configurations obtained following the theoretical treatment developed in Supporting information. Blue, red and green marks or regions correspond to out-of-plane, in-plane and island/hole configurations, respectively.

The results were sorted in three different categories: out-of-plane lamellae (**Figure 1.b-d**), in-plane lamellae and island/hole structures with an in-plane lamellar orientation (**Figure 1.a and e**), and are summarized in **Figure 1.f** for the various PS-*stat*-PMMA compositions and film thicknesses.

The domain spacing of the BCP structure was confirmed by FFT analysis of the fingerprint structure from out-of-plane lamellae and from the depth profile of the island/hole structure, confirming for each method a value close to 28 nm. It was demonstrated to be insensitive of the PS-*stat*-PMMA composition on the probed window. It is noteworthy that perforations at the free surface are visible on the AFM images of in-plane lamellar structures which could be attributed either to the rapid solvent evaporation during RTA or the formation of a metastable perforated lamellar structure. Overall, the reported phase diagram is in accordance with previous reports highlighting the importance of the interface boundary conditions (symmetric or asymmetric wetting) and the film thickness (in)commensurability with respect to the intrinsic BCP periodicity.<sup>[31-33]</sup> In particular, the lower surface energy of PMMA at high temperature leads to PMMA domains facing the air for in-plane configuration. This behavior determines in turn the asymmetric (PS-affine substrate) and symmetric (PMMA-affine substrate) wetting configurations which further dictate the incommensurability conditions for the formation of island/hole structures (i.e. asymmetric wetting  $t/L_0 \neq n$  and symmetric wetting  $t/L_0 \neq n + 0.5$ ). Additionally, the experimental results are in agreement with the theoretical treatment developed in **Supporting**

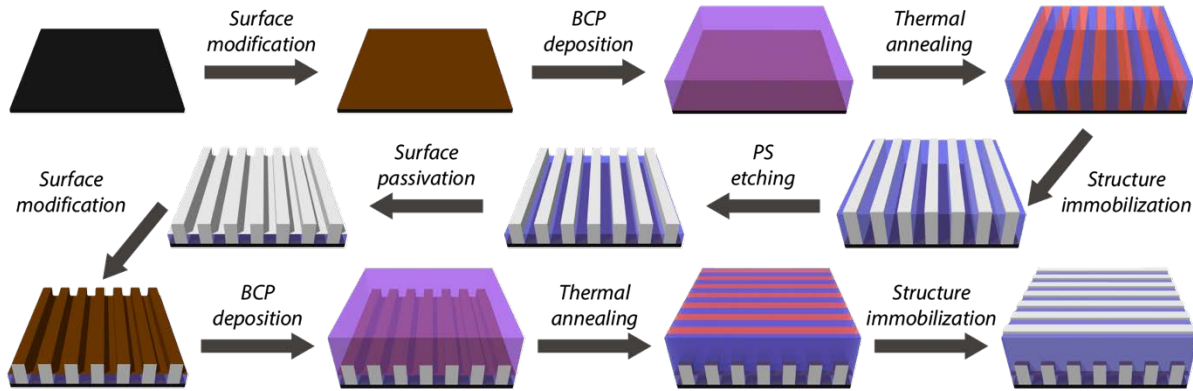
**information** as shown in **Figure 1.g**. Note that for a given film thickness, the interplay between the wetting regimes and the BCP structure commensurability (e.g.,  $t/L_0 = 1$  and symmetric (PMMA-affine grafted PS-*stat*-PMMA chains) or asymmetric (PS-affine grafted PS-*stat*-PMMA chains) wetting regimes) alternately favors or disfavors the in-plane lamellar configuration. This alternation of behaviors for every  $0.5t/L_0$  results in the zig-zag shape of the boundaries between the in-plane and out-of-plane stability regions in **Figure 1.g**. A shift from the theoretical PS-*stat*-PMMA neutral composition of  $f_{\text{PS}} = 0.5$  to higher  $f_{\text{PS}}$  is experimentally observed, which is explained by a non-linearity between the brush composition and the surface coating energy (due to effects of the end-chain groups,<sup>[34]</sup> the slight gradient composition of PS-*stat*-PMMA chains<sup>[35]</sup> and the penetration of PS and PMMA sequences of the BCP chains inside the grafted layer<sup>[29]</sup>).

Crucially, this preliminary study demonstrates that the out-of-plane lamellar orientation is achieved over a range of PS-*stat*-PMMA compositions (e.g.  $0.59 \leq f_{\text{PS}} \leq 0.77$  for  $t/L_0 \approx 1.25$ ) in line with previous studies.<sup>[36]</sup> This allows the definition of slightly PMMA- or PS- affine grafted PS-*stat*-PMMA layers (see **Table 1** for details) for which an out-of-plane orientation of the lamellar structure is retained.

**Table 1.** PS-*stat*-PMMA compositions used for the stacking process in order to tune the interfacial energy between the two  $L28$  layers.

<b>PS-<i>stat</i>-PMMA composition, <math>f_{\text{PS}}</math></b>	0.59	0.68	0.77
<b>Affinity</b>	PMMA ( $M$ )	Neutral ( $N$ )	PS ( $S$ )
<b>BCP domain orientation for <math>t/L_0 \approx 1.25</math></b>	Out-of-plane	Out-of-plane	Out-of-plane

We subsequently studied the stacking of two  $L28$  layers following a process derived from the “responsive layering” process pioneered by Rahman *et al.*<sup>[17]</sup> and summarized in **Scheme 1**.



**Scheme 1.** Process flow for the layering of two *L*28 layers taking advantage a both chemical and topographical registration fields.

Shortly, a first BCP layer is deposited by spin coating on a Si substrate modified by “fully” neutral PS-*stat*-PMMA chains ( $f_{\text{PS}} = 0.68$ ) and thermally annealed at 250 °C during 10 min using a RTA oven to promote the self-assembly. **Figure 2.a** shows a AFM image of the resulting fingerprint pattern in line with the formation of an out-of-plane lamellar structure ( $t \approx 35 \text{ nm}$ ,  $t/L_0 \approx 1.25$ ). An immobilization step of the BCP structure by sequential infiltration synthesis (SIS) is then performed through the formation of  $\text{Al}_2\text{O}_3$  in the PMMA domains followed by an  $\text{O}_2$  RIE plasma treatment which partially etched the PS domains.<sup>[37,38]</sup> Accordingly, a line & space pattern (**Figure 2.b**) with a topographical amplitude around 8 nm is formed as deduced from the analysis of the AFM topographical profile (see **Figure 2.c,d**). Next, a 1 nm thick layer of  $\text{Al}_2\text{O}_3$  is deposited on top of the immobilized pattern in order to facilitate a subsequent homogeneous grafting of PS-*stat*-PMMA chains. Finally, a second BCP layer is casted onto the line & space pattern, thermally annealed at 250 °C during 10 min and immobilized using SIS. Critically, this process enables the fine tuning of the affinity of the PS-*stat*-PMMA layer (neutral, slightly PMMA- or PS- affine) with

respect to the second BCP layer which is of crucial importance to decipher the complex interplay between topographical and chemical fields on the resulting bilayered structures.

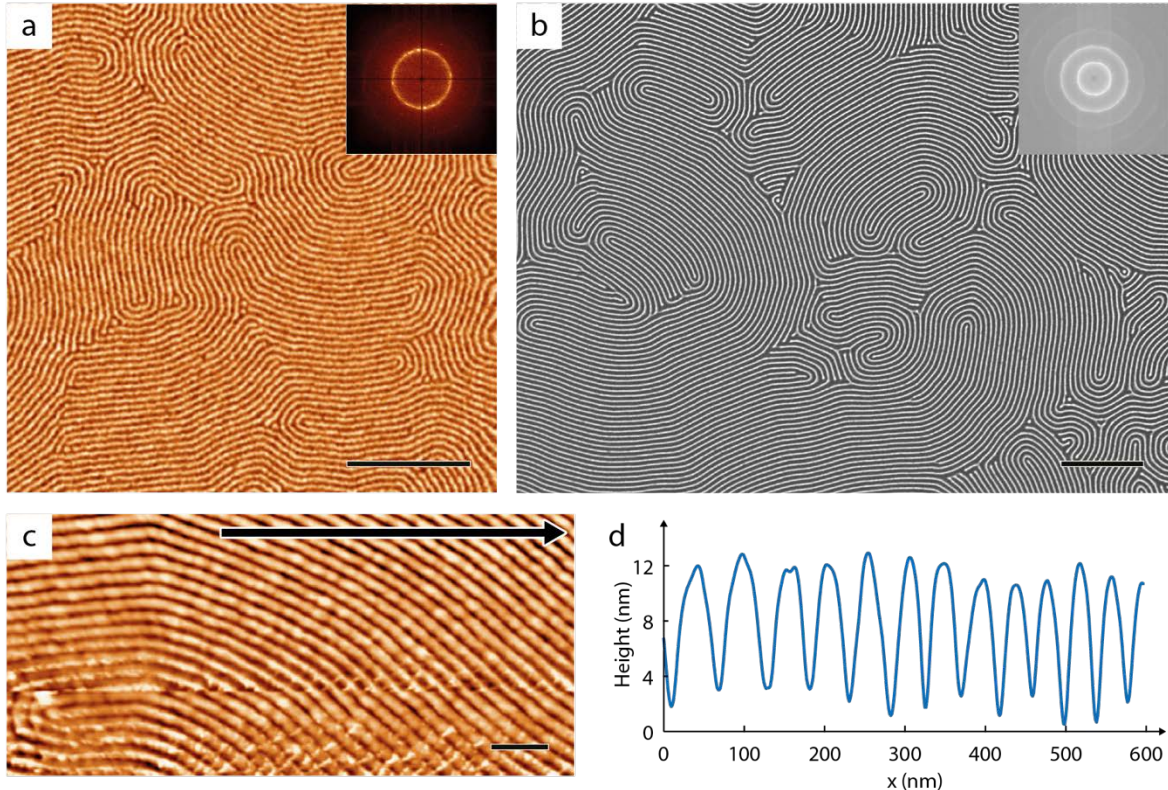


**Figure 2.** (a) AFM phase image of the nanostructured *L28* thin film after thermal annealing. (b) SEM image of the line & space pattern after SIS and O<sub>2</sub> RIE plasma treatment. Scale bars: 500 nm. Top right insets are the corresponding FFTs. (c, d) AFM height image and topographical profile taken along the arrow obtained after SIS and O<sub>2</sub> RIE plasma treatment. Scale bar: 100 nm.

Experimentally, we have studied the stacking of two *L28* layers using the aforementioned process, with the three different interfacial configurations, i.e. “fully” neutral, PMMA-affine or PS-affine (compositions of the grafted interfacial layers are summarized in **Table 1**). After the ashing of the PS domains by a prolonged O<sub>2</sub> RIE treatment, three different patterns were observed using SEM as shown in **Figure 3.a-c**, showing the top-view projections of the superimposed layers. The corresponding GISAXS 2D patterns are presented as well in **Figure 3.d-e**.

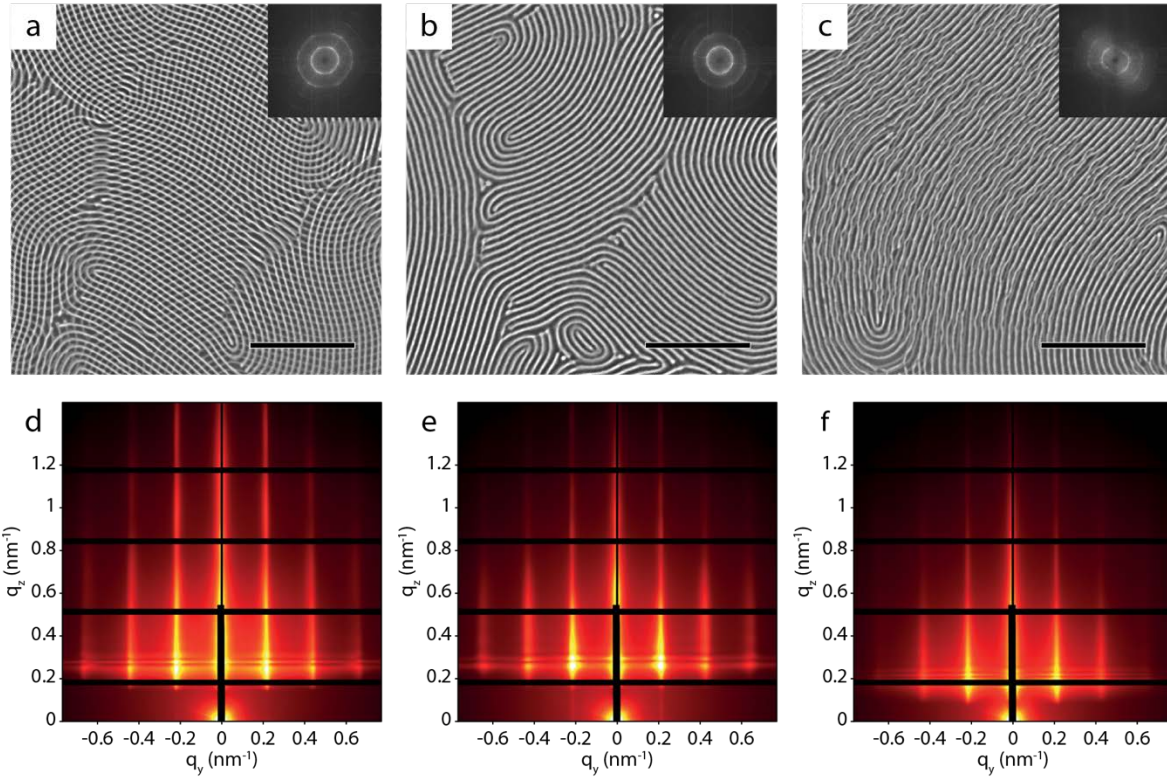


**Figure 3.** (top panel) SEM images and (bottom panel) corresponding GISAXS patterns of two stacked  $L_{28}$  layers with (a,d) neutral, (b,e) PMMA-affine and (c,f) PS-affine interfacial layers. Top right insets are the corresponding FFTs. Scale bars: 500 nm.

The “fully” neutral configuration (**Figure 3.a**) shows a decent grid pattern with an angle close to  $90^\circ$  between both layers as compared to a randomly computed one generated through the superposition of two SEM images of  $L_{28}$  layers (see **Figure S2**). However, due to the inherent defectivity of BCP self-assembly, the translational order of the underlying line & space pattern is poor, which results in multiple defects localized mainly at the grain boundaries.<sup>[39,40]</sup> The poor translational order of the first BCP layer inhibits thus the generation of a perfect orthogonal grid without further use of directed self-assembly methods (*vide infra*). The corresponding GISAXS pattern (**Figure 3.d**) is in accordance with the stacked configuration imaged by SEM. Intense

Bragg rods along  $q_y$  positioned in the characteristic  $q_y/q_y^* = 1, 2, 3$  sequence confirmed the formation of a line & space pattern with a common periodicity ( $L_0 = 28.7$  nm) for the two superimposed layers which is identical to the neat L28 domain spacing. Accordingly, the characteristic size of the top self-assembled structure does not appear to be disturbed by the chemical and topographical fields induced by the underlying Al<sub>2</sub>O<sub>3</sub> pattern. Unfortunately, the “polycrystalline” nature of the produced grid pattern (i.e. multiple angular orientations of the two grid arrays) does not permit to retrieve the angular configuration of the two superimposed line & space arrays.

**Figure 3.b** shows the structure obtained for two superimposed line & space patterns separated by a PMMA-affine interfacial layer. From such top-view image, a unique line & space pattern is observed. As the prolonged ashing by RIE is expected to remove all organic materials (i.e. the non-hybridized PS domains), we concluded to a registration between the underlying Al<sub>2</sub>O<sub>3</sub> lines and the PMMA domains of the top layer. Accordingly, a thicker Al<sub>2</sub>O<sub>3</sub> line & space array is produced after the hybridization by SIS of the second BCP layer. The GISAXS data presented in **Figure 3.e** are in agreement with this assignation as a sequence of Bragg rods such as  $q_y/q_y^* = 1, 2, 3$  is also retrieved. The periodicity of the thick line & space array was evaluated at  $L_0 = 29.3$  nm which is not significantly different with respect to the neat L28 domain spacing.

Finally, the structure obtained for a PS-affine interfacial layer (**Figure 3.c**) is harder to analyze since the top layer consists of “wavy” lines. From the top-view SEM image, the top line & space array is collinear to the bottom one, but the registration between the bottom and top arrays differs from the PMMA-affine case. As a PS-affine interfacial layer was inserted between the two arrays, this structure results from a registration between the bottom  $\text{Al}_2\text{O}_3$  lines and the PS domains of the second BCP layer. The hybridization by SIS of the PMMA domains of the second BCP layer further results in  $\text{Al}_2\text{O}_3$  lines positioned (at a different height) between the  $\text{Al}_2\text{O}_3$  lines of the first layer. The ashing step leads to a collapse of the top layer structure induced by the removal of the PS domains. We hypothesize that the resulting “wavy” pattern is related to electrostatic or capillary forces during the plasma etching step which leads to a “stitching” of the top  $\text{Al}_2\text{O}_3$  lines on the bottom  $\text{Al}_2\text{O}_3$  array at various positions as observed in **Figure 3.c**. The 2D GISAXS pattern recorded for this sample shown in **Figure 3.f** is coherent with this configuration as only two Bragg rods, inherent to a weaker translational order of the overall structure, are visible. Nevertheless, a characteristic sequence  $q_y/q_y^* = 1, 2$  is retrieved which confirms the formation of line & space arrays with a common periodicity  $L_0 = 29.3 \text{ nm}$ .

We further used grapho-epitaxy as a directed self-assembly method in order to fully highlight the complex registration of the second BCP layer with respect to the first immobilized one depending on the interfacial configuration. A thicker  $L28$  first layer ( $t \approx 160 \text{ nm}$ ) was cast onto grooved substrate previously modified with neutral PS-*stat*-PMMA chains ( $f_{\text{PS}} = 0.68$ ). After the promotion

of the self-assembly by thermal annealing, the *L*28 out-of-plane lamellae adopted an orthogonal configuration with respect to the topographical pattern as this particular arrangement is the configuration of minimal energy. This result is in accordance with previous reports evaluating the arrangement of out-of-plane lamellae in grooved substrate depending on the PS-*stat*-PMMA composition.<sup>[41,42]</sup> It is noteworthy that the use of a thicker BCP layer leads to a lamellar pattern showing a good translational order and prevents the formation of a topographical field inherent to the grooved substrate as shown in **Figure S3** (i.e. the remaining topographical pattern has an amplitude smaller than 1 nm and was considered as negligible with respect to the topographical pattern created at the time of the BCP immobilization by the combined SIS and plasma treatments).

The remaining part of the stacking process remained unchanged and **Figure 4.a-c** shows the resulting SEM images of the structures obtained after ashing the PS domains depending on the interfacial configuration. They validate the conclusions made in the previous paragraph; i.e. an orthogonal orientation of the second layer (see **Figure 4.a**) is observed if the interfacial energy between the layers is perfectly neutral (*L*28-*N*-*L*28), and a collinear one if this interfacial energy is slightly affine to one of the BCP domains. Additionally, the two line & space arrays are perfectly stacked (see **Figure 4.b**) when the surface is affine to PMMA (*L*28-*M*-*L*28), while an interfacial layer affine to PS (*L*28-*S*-*L*28) leads to a collapse of the top line & space array inside the spaces of the bottom array (see **Figure 4.c**). The results obtained using directed self-assembly methods are more robust than the previous ones, as they allow us to clearly distinguish the different stacking

configurations. In particular, three highly ordered configurations have been observed with a clear “responsive layering” mechanism depending of the interfacial energy between the two BCP layers. The next paragraph will propose different hypotheses regarding the registration mechanisms.

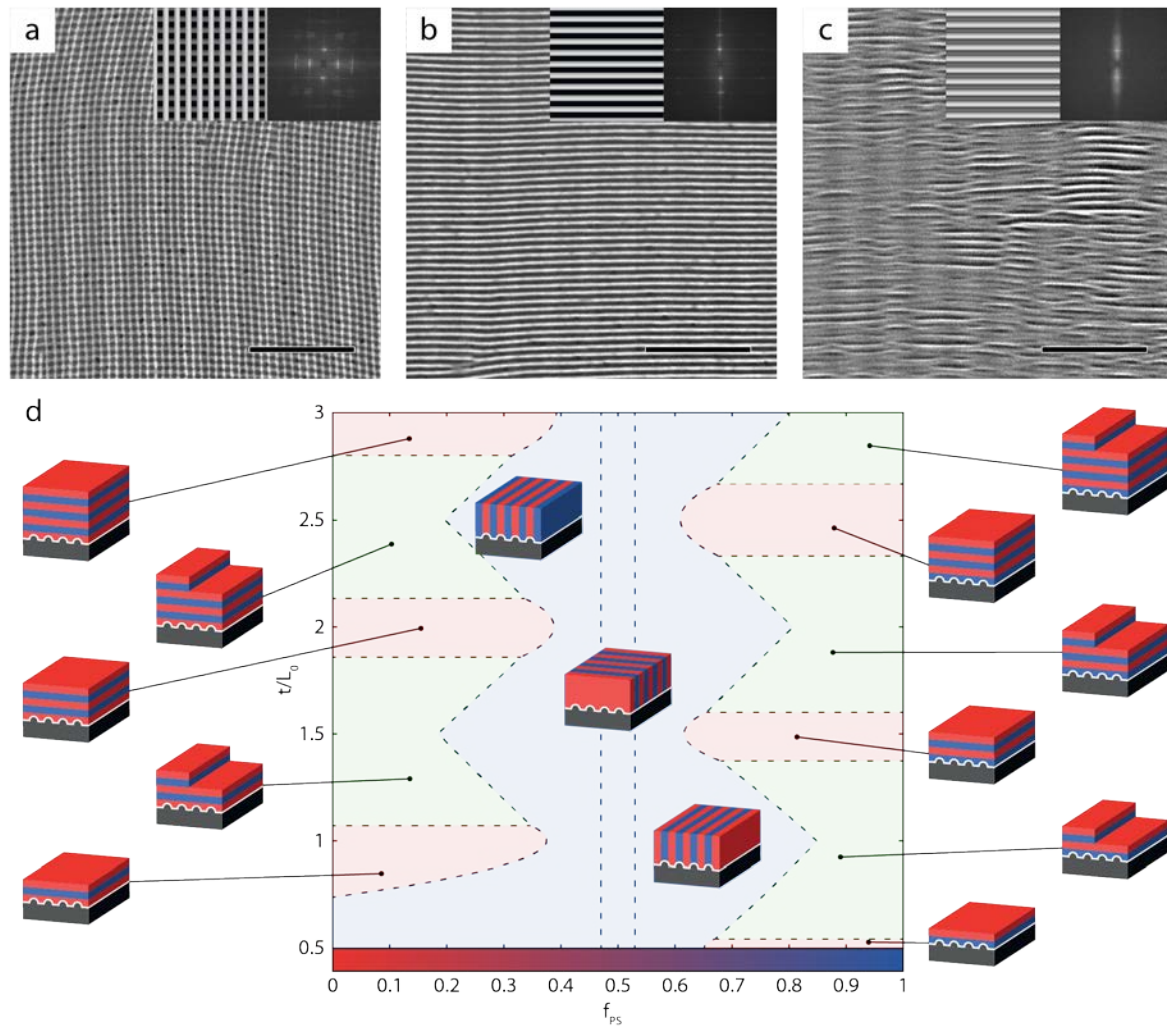


**Figure 4.** SEM images of (a)  $L28-N-L28$ , (b)  $L28-M-L28$  and (c)  $L28-S-L28$  immobilized bilayers produced on top of a grooved substrate (the initial trenches are vertically oriented on the SEM images). Top right insets are the idealized structures and FFTs of the corresponding SEM images. Scale bars: 500 nm. (d) Mapping of the different stacking configurations between the two line & space patterns obtained following the theoretical treatment developed in Supporting information.

The rationalization of these stacking configurations was pursued following two mechanisms: *i*) the formation of asymmetric surface areas due to the topographical field induced by the first immobilized layer; *ii*) the generation of chemo-epitaxy fields inherent to the disordering of PS-*b*-PMMA chains induced by a strong spatial confinement inside the 1<sup>st</sup> line & space pattern.

A first consideration is related to the increase of surface area inherent to the topography produced by the immobilization by SIS of the 1<sup>st</sup> BCP layer. Indeed, the line & space pattern is not sharp due to a gradient of composition at the interface related to the low segregation strength of the PS-*b*-PMMA system under study and the non-isotropic plasma etching process.<sup>[43,44]</sup> It is rather composed of parallel trenches with curved walls, and the resulting topographical profile has been modeled with a rectangular box ( $w \times h$ ) having rounded-shaped edges as shown in **Figure S4.a**.

In the case of an interfacial treatment of the line & space pattern by PMMA- or PS- affine interfacial layer, an energetic gain is obtained when the affine domain registers on top of the trenches, due to an excess of affine area. However, this configuration generates chain perturbations in the vicinity of the topographical pattern as shown in **Figure S4.b**, resulting in an energy penalty.

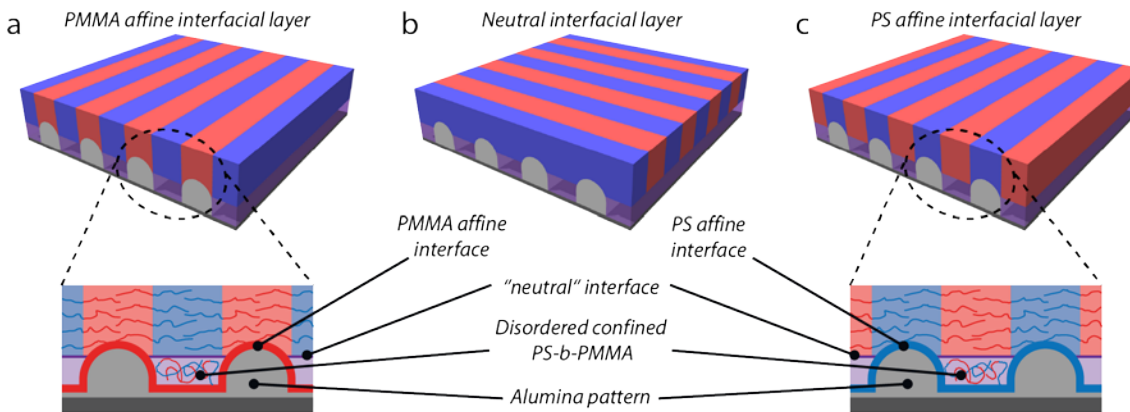
Interestingly, this penalty is completely relieved in the case of an orthogonal arrangement of the BCP domains of the 2<sup>nd</sup> layer (the substrate curvature is orthogonal to the BCP chains) which is experimentally obtained for a neutral interfacial treatment (formation of the orthogonal grid pattern after ashing). These two antagonistic energetic contributions were evaluated using a home-made code developed for the establishment of the orientational phase diagram of lamellar structures

taking into account the topographical field induced by the 1<sup>st</sup> immobilized BCP layer. It is noteworthy that the equations used to describe the lamellar structure do not take into account the perturbations of the lamellar domain shape induced by the rounded pattern. Here, we choose a patterned substrate close to the L28 experimental case, i.e. a line & space pattern with a 28 nm periodicity and a 5 nm bump height (with respect to the 8 nm experimentally probed by AFM). We further hypothesized that the effect of this topographical field is relieved for BCP layer height higher than  $2h$ . Finally, all possible orientations of the two layers were probed leading to an orientational phase diagram shown in **Figure 4.d** The orientational phase diagram is composed of two in-plane regions for strongly PMMA- or PS- affine interfacial layer compositions (not experimentally studied) and one out-of-plane window divided in three different regions depending of the affinity of the interfacial layer, i.e. orthogonal to the topographical substrate (“fully” neutral case) or parallel to the topographical substrate with either PMMA or PS domains registered above the Al<sub>2</sub>O<sub>3</sub> lines (“slightly” affine cases). The results are in complete agreement with the experimental observations previously reported in **Figure 4.a-c**. Interestingly, the overall structure of the phase diagram is not modified compared to the one obtained for a flat substrate (see **Figure 1.g**), with the same localization of the transitions between the out-of-plane, in-plane and island/hole windows. This means that the substrate patterning has a strong impact only for out-of-plane structures by orientating them orthogonally or collinearly, and does not modify the out-of-plane stability region. This can be understood as the energetical costs for chain perturbation above

the gratings related to the in-plane configuration is lower than the interfacial energetical contribution for extreme values of  $f_{\text{PS}}$ . It is noteworthy that the orthogonal configuration window between the two collinear ones is only retrieved by simulation if the bump height is below 5.5 nm. For higher values, the whole out-of-plane window has an orthogonal configuration (i.e. limiting thus chain stretching).

A second consideration to rationalize the observed stacking behavior is related to the (dis-)ordering state of the PS-*b*-PMMA chains in the strongly confined spaces between the Al<sub>2</sub>O<sub>3</sub> trenches. Indeed, both theoretical and experimental works have reported a drastic increase of  $\chi N$  value for the order-disorder transition upon confinement for a ratio between the length scale of the spatial confinement and the polymer gyration radius, of 1.4~1.5.<sup>[45,46]</sup> In our case, the trench width is half the BCP period, i.e. 14 nm, and a rough estimate of the  $R_g$  of the BCP chains is around 12.5 nm, giving a ratio effectively corresponding to a disordered state. It should be noted that the confined PS-*b*-PMMA chains could be in a non-homogenous disordered state for which local composition fluctuations with a characteristic length scale on the order of the radius of gyration of the BCP chain would prevail.<sup>[47,48]</sup> We believe that these composition fluctuations would still yield a “neutral” configuration with respect to the BCP nanostructure due to their isotropic spatial arrangement.<sup>[49]</sup> Accordingly, as shown in **Scheme 2**, we assumed that the confined PS-*b*-PMMA chains of the 2<sup>nd</sup> layer are trapped in a disordered state within the topographic spaces created by the line & space pattern from the 1<sup>st</sup> layer. This leads in turn to a “neutral” interface localized

between the  $\text{Al}_2\text{O}_3$  trenches for the BCP chains.<sup>[13]</sup> In summary, a neutral interface toward the PS and PMMA domains is generated between the  $\text{Al}_2\text{O}_3$  lines due to confinement, while the PS-*stat*-PMMA coating is still present above the  $\text{Al}_2\text{O}_3$  pattern. For PMMA- or PS- affine coatings, a self-assembly mechanism driven by chemo-epitaxy occurs, leading to an energetical gain for the collinear configurations between the two line & space patterns (see **Scheme 2**), since a domain is facing an affine interface and the other a neutral one. Alternatively, the collinear orientation for a neutral interface does not generate an energetical gain since both domains wet neutral interfaces (either from the grafting of the PS-*stat*-PMMA on the top of the  $\text{Al}_2\text{O}_3$  lines or from the disordering of the PS-*b*-PMMA inside the topographic pattern). Thus, the most stable configuration is the orthogonal orientation of the two line & space patterns, as no chain perturbation (compression or stretching) is involved in this configuration.



**Scheme 2.** Schematics of the “responsive layering” mechanism based on the disordering of PS-*b*-PMMA chains inside the topographic spaces created by the line & space pattern from the 1<sup>st</sup> layer. Self-assembled BCP layers after thermal annealing for (a) PMMA-affine, (b) “fully” neutral and (c) PS-affine interfacial layers.

In order to strengthen our analysis, dissipative particle dynamics (DPD) simulations of the iterative stacking of the two BCP layers were performed as a function of the interfacial energy of the PS-*stat*-PMMA interfacial layer (see **Table S1** for the list of interaction parameters,  $a_{ij}$  with  $i$  and  $j$  two DPD beads). We explored the out-of-plane self-assembly of A<sub>9</sub>B<sub>9</sub> chains as described in

**Supporting Information.** In our simulations, the 2<sup>nd</sup> BCP layer is constrained between a “air” layer and a patterned substrate of tunable surface energy (i.e. by grafting PS-*stat*-PMMA chains with different  $f_{\text{PS}}$ ) as depicted schematically on **Figure 5.a** (see **Figure S5** for additional details and notations). For a neutral configuration between the BCP domains and the patterned substrate (i.e.  $a_{As_1} = a_{Bs_1} = 20.44$ ), the A<sub>9</sub>B<sub>9</sub> chains self-assembles in an out-of-plane lamellar structure oriented orthogonally with respect to the patterned substrate (representing the 1<sup>st</sup> immobilized BCP layer) in line with the experimental results (see **Figure 5.b**). This result is in sharp contrast with the fingerprint pattern obtained on a flat neutral substrate (see **Figure S6**) highlighting the responsiveness of A<sub>9</sub>B<sub>9</sub> self-assembly to the chemical and topographic fields.

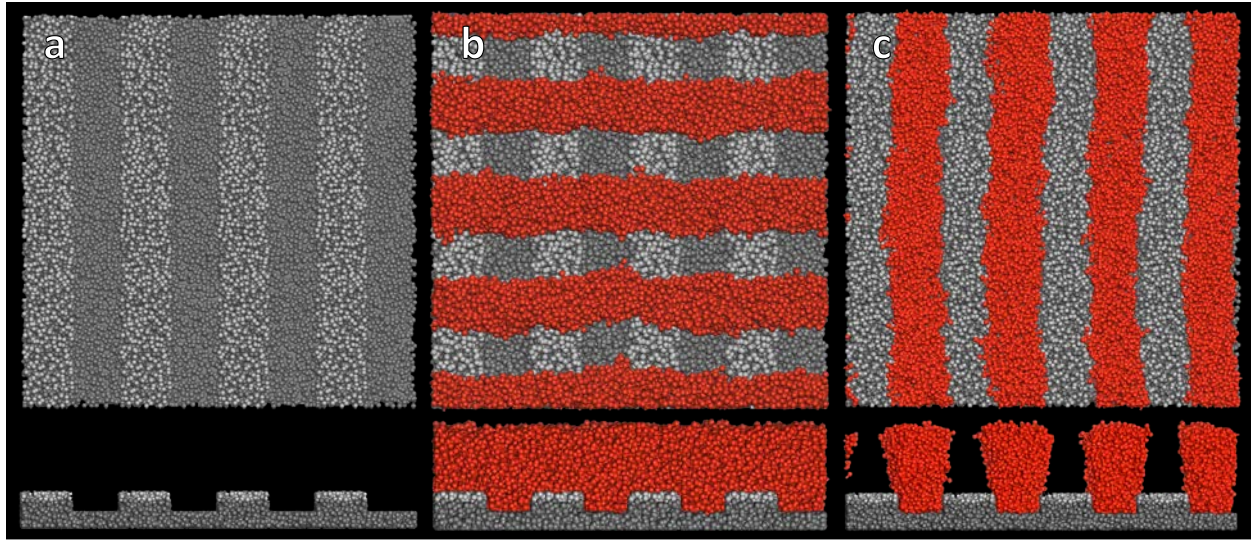


**Figure 5.** (a) Geometry of the patterned substrate corresponding to the experimental line & space pattern formed by the immobilization of the 1<sup>st</sup> BCP layer by SIS. (b) A<sub>9</sub>B<sub>9</sub> self-assembly on top of a patterned substrate fully coated by neutral beads (dark and light grey beads). (c) A<sub>9</sub>B<sub>9</sub> self-assembly on top of a patterned substrate with lines coated with an *A-affine* beads (light grey beads). The *A* and “air” beads have been removed for clarity (see Figure S7 for the self-assembled patterns with *A* and *B* beads).

When the surface of the lines corresponding to the Al<sub>2</sub>O<sub>3</sub> lines produced by the immobilization of the 1<sup>st</sup> BCP layer (i.e. light grey beads) is described by *A-affine* beads ( $a_{As_2} = 15$ ,  $a_{Bs_2} = 25.9$ , and  $a_{s_2w_2} = 15$ ), a collinear organization of the out-of-plane BCP lamellar structure is retrieved as shown in **Figure 5.c**. The *A* beads of the A<sub>9</sub>B<sub>9</sub> chains are placed on top of the *A-affine* lines while the *B* beads are repulsed in the trenches. Thus, the *B* beads fill the space on the top the interstices, even though the substrate is neutral for both blocks ( $a_{As_1} = a_{Bs_1} = 20.44$ ). In case of a *B-affine* pattern, a mirror organization of the *A-affine* model is obtained, due to the similar parametrization of the BCP beads, i.e. the *B* beads are placed on top of *B-affine* lines while the *A*

beads fill the interstices. Interestingly, the DPD simulation supports the rationalization based on the disordering of PS-*b*-PMMA chains in the voids created by the Al<sub>2</sub>O<sub>3</sub> line & space array. As shown in **Figure S7.c** for an *A*-affine pattern, some *A* beads can be observed in the confined spaces on the side-view of the A<sub>9</sub>B<sub>9</sub> self-assembled structure. **Figure S8** displays a representative horizontal cut at a height corresponding to the 1<sup>st</sup> Al<sub>2</sub>O<sub>3</sub> line & space array of the self-assembly of A<sub>9</sub>B<sub>9</sub> chains in the *A*-affine configuration. It is evident that both *A* and *B* beads are positioned in the strongly confined spaces between the Al<sub>2</sub>O<sub>3</sub> trenches even if the coarse-grained nature of DPD limits the extent of mixing. Such results clearly strengthen the rationalization based on a chemo-epitaxy field induced by the disordering of the PS-*b*-PMMA chains in the confined interstices between the Al<sub>2</sub>O<sub>3</sub> lines.

### 3 Conclusion

We have investigated the complex interplay between chemical and topographical constraints for the precise control of the registration between two stacked out-of-plane lamellar BCP layers in order to produce nano-mesh arrays. We demonstrated that the change of the interfacial energy between the nanostructured BCP films, associated to the topography inherent to the immobilization of the underneath BCP layer, leads to either an orthogonal or a collinear arrangement of the upper BCP layer with respect to the underlying one. More precisely, the definition of “slightly” affine or “fully” neutral configurations using different PS-*stat*-PMMA compositions generates three different nano-mesh arrays for which the registration of the BCP domains of the upper layer is

dictated by the conjunction of both chemical and topographical fields. These experimental results were rationalized using a free-energy model evaluating the various stacking configurations and a simple mechanism based on the disordering of PS-*b*-PMMA chains due to the strong confinement induced by the immobilized pattern was also proposed to better apprehend the observed self-assembly behavior. The various experimental configurations were further confirmed by DPD simulations using similar interfacial and topographical parametrizations, further highlighting the responsiveness of BCP self-assembly to both chemical and topographic fields. We believe this work expands the breadth of control for the directed self-assembly of stacked BCP layers by interplaying chemo-epitaxy, grapho-epitaxy and immobilization methods.

## 4 Experimental Section

*Materials.* The statistical- and block- copolymers (PS-*stat*-PMMA and PS-*b*-PMMA) were kindly provided by Arkema. The PS-*stat*-PMMA copolymers, synthesized by nitroxide-mediated radical polymerization using a BlocBuilder® MA-HEA-SG1 alkoxyamine, are characterized by  $M_n = 11.2\text{-}13.6 \text{ kg/mol}$  and  $D = 1.2\text{-}1.4$  as determined by size exclusion chromatography using PS standards for calibration. Accordingly, the PS-*stat*-PMMA copolymers are functionalized with a hydroxyl group at one end of the chain and the SG1 moiety at the other end, resulting in a grafting process involving both end-groups.<sup>[50,51]</sup> Propylene Glycol Methyl Ether Acetate (PGMEA) was purchased from Merck and used as received. Trimethylaluminium (TMA) was purchased from Strem Chemicals and used as received. Flat (100) silicon wafers were purchased from Si-Mat Materials. The patterned Si substrates (lines and spaces pattern with 60 nm depth, 70 nm width and 140 nm periodicity) were fabricated in the LTM / CEA-LETI facilities in Grenoble on 300 mm wafers. A three-layer lithography stack (193 nm lithography resist on silicon-containing antireflective coating (SiARC) and spin-on carbon (SOC) layers) was exposed in a projection photo-lithography tool and dry-etched using different plasma mixtures. SiARC was opened using a combination of CHF<sub>4</sub> and Ar gases, SOC was etched using a combination of HBr, O<sub>2</sub>, and N<sub>2</sub> gases and Si was etched using a combination of HBr, Cl<sub>2</sub>, and O<sub>2</sub> gases. Finally, organic resist residues were removed in an oxygen containing plasma. Wafers were cut to approximately 1 x 1 cm<sup>2</sup> samples.

*Preparation of the BCP bilayers.* Si wafers or grooved substrates were cleaned in a PGMEA bath followed by a drying step with a N<sub>2</sub> flow. The grafted PS-*stat*-PMMA layers were produced by spin-coating (1500 rpm) a 2 wt% solution in PGEMA onto the Si wafers or the grooved substrates followed by a thermal annealing step at 250 °C for 5 min. The ungrafted PS-*stat*-PMMA chains

were subsequently rinsed in a PGEMA bath. Thereafter, a PS-*b*-PMMA solution in PGEMA (1.5 wt% for  $t/L_0 = 1.25$ ) was deposited at 1500 rpm and thermally annealed at 250 °C for 10 min using a rapid thermal annealing (RTA) system (Jipelec ECM JetLight) under N<sub>2</sub> atmosphere. Sequential Infiltration Synthesis (SIS) was then performed using an ALD tool (Ultratech SAVANNAH G2) in exposure mode. The sequence used in this study consists of two infiltration cycles composed of two exposures of TMA vapor at 85 °C during 60 s followed by two exposures of H<sub>2</sub>O vapor at 85 °C during 60 s. Each exposure was followed by 10 sec N<sub>2</sub> flow purge to remove the excess of precursors. After SIS, the etching of the PS domains was performed with an O<sub>2</sub> Reactive Ion Etching (RIE) plasma (Plasmionique Flarion RF-Series) (40 sccm O<sub>2</sub>, 40 W, 40 sec). The immobilization process of this first nanostructured BCP film also yields to the generation of a stable platform for the subsequent tuning of interfacial energy between the stacked layers. A passivation of the immobilized Al<sub>2</sub>O<sub>3</sub> pattern was conducted after the plasma etching step in order to deposit a thin Al<sub>2</sub>O<sub>3</sub> layer on top of the first layer. It further allows the modification of the surface energy by grafting a PS-*stat*-PMMA layer onto this continuous oxide layer. Experimentally, we opted to perform 10 ALD cycles using sequential TMA and H<sub>2</sub>O exposures at 85 °C leading to the formation of a  $\approx$  1 nm thick Al<sub>2</sub>O<sub>3</sub> layer.<sup>[52]</sup> The surface modification *via* the grafting of PS-*stat*-PMMA chains was subsequently performed on the passivated surface using the same protocol as the one reported for the Si wafers. A second BCP layer was then spin-coated on top of the Al<sub>2</sub>O<sub>3</sub> pattern, annealed at 250 °C for 10 min using the RTA system and treated by SIS using the same protocol as the 1<sup>st</sup> BCP layer. Finally, a ashing step using a prolonged RIE treatment (40 sccm O<sub>2</sub>, 20 W, 180 sec) was used to remove the PS domains without deteriorating the overall Al<sub>2</sub>O<sub>3</sub> structure.

*Atomic Force Microscope (AFM).* AFM images in tapping mode were obtained using a Dimension FastScan (Bruker). Silicon cantilevers (Fastscan-A) with a nominal tip radius of 5 nm, a spring constant about 18 N.m<sup>-1</sup> and a resonance frequency of about 1.4 kHz were used.

*Scanning Electron Microscope (SEM).* SEM images were obtained using a Jeol 7800-E Prime at a high acceleration voltage (15 kV) in the super high resolution gentle beam (GBSH) mode.

*Grazing incidence small X-ray scattering (GISAXS).* The GISAXS measurements were carried out on SIRIUS station (Soft Interfaces and Resonant Investigation on Undulator Source) at the SOLEIL synchrotron in Gif-sur-Yvette (France) using a beam energy of 8 keV.<sup>[53]</sup> The sample-to-detector distance was set to 4445 mm. The incidence angle was fixed at 0.18° for all measurements. 2D scattering patterns were collected with a PILATUS 1M Dectris detector with a vertical beam stop in front of the detector and were reduced using a home-made code, where  $q_y = 2\pi/\lambda[\sin(2\theta_f)\cos(\alpha_f)]$  and  $q_z = 2\pi/\lambda[\sin(\alpha_f) + \sin(\alpha_i)]$  are the modulus of the scattering vectors in the direction parallel and perpendicular to the substrate plane and  $\alpha_i$ ,  $2\theta_f$  and  $\alpha_f$  are the incident and scattering angles in the horizontal and vertical directions, respectively.

*Mapping of the configurations of lamellar structures in thin films.* A simple predictive treatment has been developed to map out the configurations of lamellar BCP structures with respect to the film thickness and interface wetting.<sup>[54,55]</sup> The energetical aspects considered in this treatment are: *i*) the substrate interfacial energy, corresponding to the interaction between the BCP film and the substrate surface; *ii*) the free surface interfacial energy, which represents the interactions between the BCP film and air; *iii*) the conformational constraints of the BCP chains (i.e. stretching or compression due to the chain distortion away from its equilibrium length, and repulsive interactions between the chains due to the chemical difference between each block). The details of the treatment are available in **Supporting Information**.

*Dissipative particle dynamics (DPD).* The DPD simulation method used in this study is based on the DPD method reported by Huang and Alexander-Katz for BCP directed self-assembly.<sup>[56]</sup> The treatment developed for this study is further detailed in **Supporting Information**.

## **Acknowledgements**

N.D. is grateful for a financial support from the University of Bordeaux (Ph.D. fellowship). This work was performed within the framework of the Equipex ELORPrintTec ANR-10-EQPX-28-01 with the help of the French state's Initiative d'Excellence Bordeaux IdEx ANR-10-IDEX-003-02. This work was partially supported by the European Union Horizon 2020 research and innovation program under grant agreement #760915 (SUN-PILOT project) and the REX-7 project from Région Rhône Alpes and BPI France. Arkema is acknowledged for supplying the PS-*stat*-PMMA and PS-*b*-PMMA materials. The authors would like to further acknowledge SOLEIL for provision of synchrotron radiation facilities at the SIRIUS station and tank Dr. Philippe Fontaine for its help during the GISAXS experiments.

- [1] I. Gunkel, *Small* **2018**, *14*, 1802872.
- [2] C. Cummins, R. Lundy, J. J. Walsh, V. Ponsinet, G. Fleury, M. A. Morris, *Nano Today* **2020**, *35*, 100936.
- [3] A. Alvarez-Fernandez, C. Cummins, M. Saba, U. Steiner, G. Fleury, V. Ponsinet, S. Guldin, *Adv. Opt. Mater.* **2021**, *9*, 2100175.
- [4] A. A. Kulkarni, G. S. Doerk, *Nanotechnology* **2022**, *33*, 292001.
- [5] F. S. Bates, G. H. Fredrickson, *Phys. Today* **1999**, *52*, 32.
- [6] M. J. Fasolka, A. M. Mayes, *Annu. Rev. Mater. Res.* **2001**, *31*, 323.
- [7] M. Luo, T. H. Epps, *Macromolecules* **2013**, *46*, 7567.
- [8] C. Cummins, T. Ghoshal, J. D. Holmes, M. A. Morris, *Adv. Mater.* **2016**, *28*, 5586.
- [9] C. A. Ross, K. K. Berggren, J. Y. Cheng, Y. S. Jung, J. B. Chang, *Adv. Mater.* **2014**, *26*, 4386.
- [10] G. S. Doerk, K. G. Yager, *Mol. Syst. Des. Eng.* **2017**, *2*, 518.
- [11] J. H. Kim, H. M. Jin, G. G. Yang, K. H. Han, T. Yun, J. Y. Shin, S. Jeong, S. O. Kim, *Adv. Funct. Mater.* **2019**, 1902049.
- [12] N. Demazy, C. Cummins, K. Aissou, G. Fleury, *Adv. Mater. Interfaces* **2020**, *7*, 1901747.
- [13] J. Oh, H. S. Suh, Y. Ko, Y. Nah, J.-C. Lee, B. Yeom, K. Char, C. A. Ross, J. G. Son, *Nat. Commun.* **2019**, *10*, 2912.
- [14] X. Chevalier, C. Gomes Correia, G. Pound-Lana, P. Bézard, M. Sérégé, C. Petit-Etienne, G. Gay, G. Cunge, B. Cabannes-Boué, C. Nicolet, C. Navarro, I. Cayrefourcq, M. Müller, G. Hadzioannou, I. Iliopoulos, G. Fleury, M. Zelsmann, *ACS Appl. Mater. Interfaces* **2021**, *13*, 11224.
- [15] J. G. Son, A. F. Hannon, K. W. Gotrik, A. Alexander-Katz, C. a Ross, *Adv. Mater.* **2011**, *23*, 634.
- [16] P. W. Majewski, A. Rahman, C. T. Black, K. G. Yager, *Nat. Commun.* **2015**, *6*, 7448.
- [17] A. Rahman, P. W. Majewski, G. Doerk, C. T. Black, K. G. Yager, *Nat. Commun.* **2016**, *7*, 13988.
- [18] C. Jin, B. C. Olsen, N. L. Y. Wu, E. J. Luber, J. M. Buriak, *Langmuir* **2016**, *32*, 5890.
- [19] A. Tavakkoli K. G., S. M. Nicaise, K. R. Gadelrab, A. Alexander-Katz, C. A. Ross, K. K. Berggren, *Nat. Commun.* **2016**, *7*, 10518.
- [20] L. Cheng, J. W. Simonaitis, K. R. Gadelrab, M. Tahir, Y. Ding, A. Alexander-Katz, C. A. Ross, *Small* **2020**, *16*, 1905509.
- [21] A. Subramanian, G. Doerk, K. Kisslinger, D. H. Yi, R. B. Grubbs, C. Y. Nam, *Nanoscale* **2019**, *11*, 9533.
- [22] E. Kim, C. Shin, H. Ahn, D. Y. Ryu, J. Bang, C. J. Hawker, T. P. Russell, *Soft Matter* **2008**, *4*, 475.
- [23] H. Jung, D. Hwang, E. Kim, B.-J. Kim, W. B. Lee, J. E. Poelma, J. Kim, C. J. Hawker, J.

- Huh, D. Y. Ryu, J. Bang, *ACS Nano* **2011**, *5*, 6164.
- [24] J. W. Jeong, W. I. Park, L.-M. M. Do, J.-H. H. Park, T.-H. H. Kim, G. Chae, Y. S. Jung, *Adv. Mater.* **2012**, *24*, 3526.
- [25] A. A. Abate, G. T. Vu, A. D. Pezzutti, N. A. García, R. L. Davis, F. Schmid, R. A. Register, D. A. Vega, *Macromolecules* **2016**, *49*, 7588.
- [26] A. Knoll, A. Horvat, K. S. Lyakhova, G. Krausch, G. J. A. Sevink, A. V Zvelindovsky, R. Magerle, *Phys. Rev. Lett.* **2002**, *89*, 035501.
- [27] S. Ji, L. Wan, C. C. Liu, P. F. Nealey, *Prog. Polym. Sci.* **2016**, *54–55*, 76.
- [28] C. Jin, B. C. Olsen, E. J. Luber, J. M. Buriak, *ACS Nano* **2017**, *11*, 3237.
- [29] P. Mansky, Y. Lui, E. Huang, T. P. Russell, C. J. Hawker, *Science* **1997**, *275*, 1458.
- [30] P. Mansky, T. P. Russell, C. J. Hawker, M. Pitsikalis, J. Mays, *Macromolecules* **1997**, *30*, 6810.
- [31] E. Huang, S. Pruzinsky, T. P. Russell, J. Mays, C. J. Hawker, *Macromolecules* **1999**, *32*, 5299.
- [32] S. Kim, C. M. Bates, A. Thio, J. D. Cushen, C. J. Ellison, C. G. Willson, F. S. Bates, *ACS Nano* **2013**, *7*, 9905.
- [33] M. J. Maher, C. M. Bates, G. Blachut, S. Sirard, J. L. Self, M. C. Carlson, L. M. Dean, J. D. Cushen, W. J. Durand, C. O. Hayes, C. J. Ellison, C. G. Willson, *Chem. Mater.* **2014**, *26*, 1471.
- [34] E. Han, K. O. Stuen, Y. H. La, P. F. Nealey, P. Gopalan, *Macromolecules* **2008**, *41*, 9090.
- [35] R. Leicht, J. Fuhrmann, *J. Polym. Sci. Polym. Chem. Ed.* **1983**, *21*, 2215.
- [36] S. Ham, C. Shin, E. Kim, D. Y. Ryu, U. Jeong, T. P. Russell, C. J. Hawker, *Macromolecules* **2008**, *41*, 6431.
- [37] Q. Peng, Y. C. Tseng, S. B. Darling, J. W. Elam, *ACS Nano* **2011**, *5*, 4600.
- [38] M. Biswas, J. A. Libera, S. B. Darling, J. W. Elam, *Chem. Mater.* **2014**, *26*, 6135.
- [39] S. O. Kim, B. H. Kim, K. Kim, C. M. Koo, M. P. Stoykovich, P. F. Nealey, H. H. Solak, *Macromolecules* **2006**, *39*, 5466.
- [40] S. M. Hur, V. Thapar, A. Ramírez-Hernández, P. F. Nealey, J. J. de Pablo, *ACS Nano* **2018**, *12*, 9974.
- [41] E. Han, H. Kang, C. C. Liu, P. F. Nealey, P. Gopalan, *Adv. Mater.* **2010**, *22*, 4325.
- [42] S.-M. Park, M. P. Stoykovich, R. Ruiz, Y. Zhang, C. T. Black, P. F. Nealey, *Adv. Mater.* **2007**, *19*, 607.
- [43] M. W. Matsen, M. Schick, *Curr. Opin. Colloid Interface Sci.* **1996**, *1*, 329.
- [44] D. F. Sunday, M. J. Maher, A. F. Hannon, C. D. Liman, S. Tein, G. Blachut, Y. Asano, C. J. Ellison, C. G. Willson, R. J. Kline, *Macromolecules* **2018**, *51*, 173.
- [45] B. Miao, D. Yan, C. C. Han, A.-C. Shi, *J. Chem. Phys.* **2006**, *124*, 144902.

- [46] A. Alexander-Katz, G. H. Fredrickson, *Macromolecules* **2007**, *40*, 4075.
- [47] S. A. Brazovskii, *Sov. Phys. JETP* **1975**, *41*, 85.
- [48] G. H. Fredrickson, E. Helfand, *J. Chem. Phys.* **1998**, *87*, 697.
- [49] F. S. Bates, J. H. Rosedale, G. H. Fredrickson, *J. Chem. Phys.* **1990**, *92*, 6255.
- [50] C. Navarro, S. Magnet, X. Chevalier, R. Tiron, *Method for Preparing Surfaces*, **2012**, WO2012140383.
- [51] R. Chiarcos, V. Gianotti, M. Cossi, A. Zoccante, D. Antonioli, K. Sparnacci, M. Laus, F. E. Caligiore, M. Perego, *ACS Appl. Electron. Mater.* **2019**, *1*, 1807.
- [52] D. Pan, L. Ma, Y. Xie, T. C. Jen, C. Yuan, *J. Vac. Sci. Technol. A Vacuum, Surfaces, Film.* **2015**, *33*, 021511.
- [53] P. Fontaine, G. Ciatto, N. Aubert, M. Goldmann, *Sci. Adv. Mater.* **2014**, *6*, 2312.
- [54] M. S. Turner, *Phys. Rev. Lett.* **1992**, *69*, 1788.
- [55] D. G. Walton, G. J. Kellogg, A. M. Mayes, P. Lambooy, T. P. Russell, *Macromolecules* **1994**, *27*, 6225.
- [56] H. Huang, A. Alexander-Katz, *J. Chem. Phys.* **2019**, *151*, 154905.

## Table of Contents

A subtle combination of chemical and topographical fields is used to demonstrate design rules for the controlled registration between stacked block copolymer thin films. The change in the interfacial energy between the nanostructured layers, coupled with the topography inherent to the immobilization process, induces an orthogonal or collinear orientation of the top BCP layer with respect to the underlying one.

